RSC Advances

PAPER

View Article Online
View Journal | View Issue

Cite this: *RSC Adv.*, 2019, **9**, 7551

First principles study for band engineering of $KNbO_3$ with 3d transition metal substitution†

Yunting Liang [abc] and Guosheng Shao [*abc]

First principles calculations in the framework of density functional theory (DFT) were performed to tune the electronic structures of wide gap $KNbO_3$ through 3d transition metal substitution, using PBE and HSE06 functionals for the exchange correlation potentials. While PBE functionals are suitable for structural and energetic properties, HSE06 is more reliable for band structure calculations. Impurity bands owing to V, Mn, or Fe are present in the forbidden gap, leading to effective reduction of optical gaps *via* multiple wavelength absorption. It is discovered that Ti and Cr doped systems are suitable for n type transparent conducting oxide (TCO), the Ni doped system for highly desirable p type TCO, and the Cu doped system is an excellent candidate for p type optical absorber layers. This work provides a systematic and overall perspective on the effects and associated mechanisms of transition metal doping or alloying, thus helping exploitation of perovskite oxides as potential key materials for photovoltaic and transparent photonic applications.

Received 12th January 2019
Accepted 13th February 2019

DOI: 10.1039/c9ra00289h

rsc.li/rsc-advances

Introduction

As a most promising renewable energy source to address the energy crisis due to limited fossil fuel resources and related environmental damage, current silicon wafer based solar cells have been extensively exploited for decades, with a maximum energy conversion efficiency of only about 25% due to the Shockley–Queisser (SQ) limit.[1,2] Thin film solar cells using hybrid perovskite $CH_3NH_3PbI_3$ as the optical absorbing layer were shown to be promising as a low-cost technology, with efficiency beyond 22% having been achieved over a short time since initial work in 2009, largely attributed to a suitable bandgap and high carrier mobility.[3,4] However, there are two obvious setbacks for $CH_3NH_3PbI_3$ solar cells, which hinder their wide application. One concern lies in material instability in the ambient environment, and the other comes from potential pollution from lead ions. It is therefore necessary to develop perovskite materials which are stable, abundant and environmentally friendly, thus making them desirable for the next generation of high-performance thin film solar cells.

Recently researchers have made further efforts in exploring inorganic perovskite $CsPbI_3$ for photovoltaic application, through tentative substitutions of Pb to avoid toxicity and iodine to address instability issues.[5–7] Previous work[8–27] suggested that inorganic and nontoxic multiferroic perovskite semiconductors, particularly oxide based systems, could be better alternatives for solar cell applications, owing to their high stability with adjustable bandgap and carrier concentrations through doping or alloying. Generally, a typical wide gap perovskite is based on the configuration of ABO_3, with A being an alkaline-earth metal or alkali metal element and B a transition metal. Generally, d-orbitals from the B site defines the position of the conduction band minimum (CBM) and oxygen 2p states sitting at the valence band maximum (VBM). Such a rule of thumb has been widely exploited, leading to effective doping or alloying in $ATiO_3$ (A = Ca, Sr and Ba),[8–13] $KNbO_3$ (ref. 14, 15 and 18–27) and $BiFeO_3$.[16,17]

Among these oxide perovskites, effective alloying or doping effect was achieved in $KNbO_3$ (for the sake of simplicity, we use doping to refer incorporation of impurity element in this work). As is well recognized, first principle studies can provide very useful insights on alloying or doping effects, so that effective tuning of fundamental electronic structures and associated properties can be realized cost effectively through fundamental guidance.[18] Grinberg *et al.*[19] modelled alloying effect in $[KNbO_3]_{1-x}[BaNi_{1/2}Nb_{1/2}O_{3-\delta}]_x$, namely KBNNO, and then prepared materials with $x = 0.1$–0.5 to obtain bandgaps of 1.1–2.0 eV suitable for solar cells. Their theoretical calculations revealed that the filled Ni 3d states at the VBM played a crucial role in lowering the bandgap, which was confirmed by their experimental work. Subsequent experimental work by Zhou *et al.*[20] showed with XRD analysis that the KBNNO crystals underwent phase transitions from orthorhombic to cubic

[a]*School of Materials Science and Engineering, Zhengzhou University, Zhengzhou 450001, China. E-mail: gsshao@zzu.edu.cn*

[b]*State Center for International Cooperation on Designer Low-carbon & Environmental Materials (CDLCEM), Zhengzhou University, 100 Kexue Avenue, Zhengzhou 450001, China*

[c]*Zhengzhou Materials Genome Institute (ZMGI), Zhongyuanzhigu, Building 2, Xingyang 450100, China*

† Electronic supplementary information (ESI) available. See DOI: 10.1039/c9ra00289h

structure with x increasing from 0 to 0.3. Their UV experiment showed the same range of reduced bandgap with Grinberg's results. They then prepared $Ba(Ti_{0.75}Ce_{0.125}Ni_{0.125})O_{3-\delta}$ (BTCN) thin film that exhibited a cubic perovskite structure, albeit being deviated from the ideal *Pm3m* space group. They concluded that the Ni octahedral energy splitting in BTCN resulted in bandgap reduction.[21] On the basis of the substitutional model by Grinberg *et al.*, various co-doping efforts were then made experimentally, covering Ba + Fe,[22] Ba + Co,[23,24] Ba + Ni[25–27] and Ba + Zn[28] in $KNbO_3$, though the impacts of the subsequent work was limited due to the lack of systematic understanding for electronic structures.

Another important component of a thin-film photovoltaic cell is a transparent conductive oxide (TCO), which is typically of a wide bandgap over 3.0 eV with effective doping to deliver high electrical conductivity without losing transmittance to visible and infrared light. As is widely recognized, the current TCO coatings are dominated by Sn-doped indium oxide (ITO), which is expensive with very limited indium resources.[29,30] While FTO ($F–SnO_2$) has rivalling TCO performance, there is toxic issue from using fluorine for doping.[31] Another candidate AZO (Al–ZnO) suffers from the setback of low material stability.[32] Great efforts are therefore needed to deliver alternative TCO candidates using low-cost materials with large and green resources, so that sustainable alternative materials can be used to meet the ever-increasing need of TCO coatings.[33] It is envisaged that wide gap perovskite oxides could offer competitive TCO solutions, owing to the large variety of compositional choices and inherited high carrier mobility, although efforts in this regard have been rather limited.[34,35]

This work is dedicated to provide a fundamental road map in guiding doping oxide perovskite with 3d transition metals. The work covers doping/alloying effect though introduction of each of the 3d elements into $BaNb_{2/3}B'_{1/3}O_3$, so as to obtain a perspective view on the interactive role of d-orbitals towards band engineering. We find that introduction of 3d element demonstrates three distinctive effects: (a) shifting the Fermi level towards either the CBM or the VBM for effective doping into degenerated n- or p-type semiconductors; (b) introduction of mid-gap bands to permit multi-wavelength absorption; and (c) change of bandgap values through alloying.

Method

First principles modelling was carried out in the framework of the density functional theory (DFT), using the Vienna Ab initio Simulation Package code (VASP) with a plane-wave basis set described by the projector augmented wave (PAW) method for the ionic potentials.[36] It is well established that functionals from generalized gradient approximation (GGA) underestimate bandgap values for transition metal oxides due to omission of the nonlocal effect, even though they are fundamentally adequate for structure-energy investigation at the ground states (*e.g.* formation energy, lattice parameters, and semi-quantitatively, as well as magnetism owing to spin polarization).[37–41] Here we used the PBE functional[42,43] for efficient structure-energy modelling to determine the stable structures of doped/alloyed materials. For dependable band structures, we adopted the well tested HSE06 functionals.[44–47] The screen parameter (w) for the HSE06 model is 0.2, which defines a short range ($2/w$) for mixing of a quarter of HF with PBE for reduced computational cost (no screening corresponds to PBE0). It was shown in previous work that HSE06 was adequate to predict a band gap of 3.10 eV for the orthorhombic $KNbO_3$ perovskite phase,[48] being in excellent agreement with the experimental value of 3.23 eV.[49]

An energy cut-off of 520 eV was adopted for the PAW-PBE pseudopotentials, as recommended in the VASP manual (1.3 times of default upper cut-off energy),[50] Table S1.† A criterion of 0.01 eV $Å^{-1}$ per atom was chosen for adequate relaxation of the Hellmann–Feynman residual forces, together with a Gaussian smearing width of 0.05 eV to quicken convergence. The adopted high symmetry paths for cubic $KNbO_3$ were X (0.5, 0, 0), R (0.5, 0.5, 0.5), M (0.5, 0.5, 0), G (0, 0, 0) and R (0.5, 0.5, 0.5). K mesh was defined with spacing below 0.03 $Å^{-1}$ for structure-energy calculations, and a finer K-mesh was used for electronic structures (spacing below 0.04 $Å^{-1}$).

The $2 \times 2 \times 2$ super cell of $KNbO_3$ unit cells (40 atoms) was used to study doping effect on the Nb site, with the doping model of solid solution $(KNbO_3)_{5/8}$-$(BaNb_{2/3}B'_{1/3}O_3)_{3/8}$, as shown in Fig. 1. In such a structural model, a transition metal dopant only replaces Nb in one of the basic $KNbO_3$ cells, with Ba substituting half of K sites at the face and edge centres on the basal planes of the supercell, to balance charge and enhance structural stability. The corresponding doping concentration for the Nb sites is thus 12.5%.

Results and discussion

Geometrical factors

Generally, the tolerance factor and octahedron factor are two key indices for predicting the stability of crystal structures from ionic radius aspect, which can be used as initial indicators in

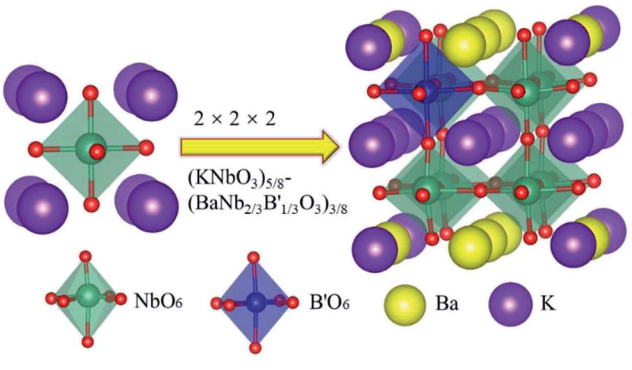

Fig. 1 $2 \times 2 \times 2$ supercell of $(KNbO_3)_{5/8}$-$(BaNb_{2/3}B'_{1/3}O_3)_{3/8}$ model with 8 cubic perovskite unit cells. In the left unit cell, a centre Nb atom (green) is bonded to six O atoms (red) to form a NbO_6 octahedron unit, while K atoms (purple) occupy the corners of the cube. In the right supercell, one dopant atom B′ (blue) replaces one centre Nb atom among eight NbO_6 octahedron cages, with Ba atoms (yellow) substituting K atoms at half of the face and edge centred sites on the basal planes of the supercell.

selecting suitable dopants or alloying elements. The tolerance factor (t) is defined by the following formula (1):[51]

$$R_A + R_O = \sqrt{2}(R_B + R_O)t \quad (1)$$

where R_A, R_B and R_O respectively representing A, B and O ion radius in ABO_3 structure, with A atoms at the corners of a cubic lattice, B sitting at the cubic centre, and O occupying face centres. The stability of the BO_6 octahedron is thus essential to sustain a cubic perovskite structure. Normally the t value for stable cubic structure of perovskite varies from 0.91 to 1.10. The stability of BO_6 octahedron cage is described by the octahedron factor R_B/R_O,[52] which is normally between 0.414 and 0.732 for stable octahedrons. When it is less than 0.414, it leads to O–B–O being too close to each other thus resulting in electrostatic repulsion from O atoms. On the other hand, a BO_6 octahedron cage will be turned into a BO_8 cube cage when R_B/R_O is greater than 0.732.

Here Shannon radii are adopted, with K radius being 1.64 Å and Ba 1.61 Å for the A site with 12 coordination, and Nb-0.64 Å and O-1.4 Å for sites with 6 coordination. Ionic radii for transition metals are plotted in Fig. 2. While increased filling of d-orbitals leads to an overall trend of reduced ionic diameter for the 3d transition metals, magnetostriction especially for V, Cr, Mn and Co due to unpaired 3d electrons is behind abnormal deviation from the general trends (Table 1). It is worth pointing out that while DFT with PBE has been widely used for assessment of magnetism, non-local effects in the XC functionals and associated electronic structures would need to be considered for greater accuracy. All 3d elements meet the stability request in the tolerance factor (0.91–1.10) and octahedron factor (0.414–0.732). These two factors show the corresponding trends with radius trend.

Stable structures of doped supercells are obtained by geometric relaxation. The resultant supercell deviates from the cubic structure slightly, with c-axis being slightly larger than a (Table S2†). Overall the resultant supercells expand due to substitution of one eighth of Nb by other 3d elements, which is consistent with B′–O bond length increasing with the atomic number of the dopant, Fig. 3a. This is understandable as the electronegativity of 3d elements generally increases, thus impacting ionic interaction between B′ and O. The abnormality for Mn and Fe doped systems is associated with their rather different magnetic momentums (Table 1), as higher spin polarization causes lattice extension, and *vice versa*.[53] Also, with increasing filling of 3d shell of dopant, the bond angle of O–B′–O chain gradually deviates from standard 180° due to lattice distortion with Mn and Zn showing the maximum 15° offset, as shown in Fig. 3b. The same situation happens in the octahedral tilt angle between NbO_6 and $B'O_6$ octahedrons with the increasing distortion, Fig. 3c.

The calculated formation energy is used to predict the stability of doped systems. The formation energy for B′ substitution of one Nb is termed as:

$$E_f = -(E_{total} - E_{KNbO_3} - E_{B'}) \quad (2)$$

where E_{total} represents total energy of doped system, E_{KNbO_3} is the energy of doped system with a Nb vacancy, and $E_{B'}$ is the total energy of simple B′ substance.[54] It is noticed that the formation energy decreases from Ti to Cr with predicted stable structures from stronger B′–O bonding, but it then increases continuously from Mn to Zn with increasingly filled 3d shell, Fig. 3d. The total energy from DFT-PBE calculations increases gradually with increasing atomic number of dopants, which is consistent with extended lattices in Table S2.†

Lattice parameters for all doped systems are listed in Table S2.† Because Shannon radii of all chosen transition metals are bigger than parent centre atom Nb, so that lattice parameters of doped structures are all larger than undoped $KNbO_3$, with the maximum enlargement by 0.252 Å in Mn doped lattice. The slight tetragonality (c/a) in doped structures is consistent with acceptable geometrical factors for stabilized perovskite structures.

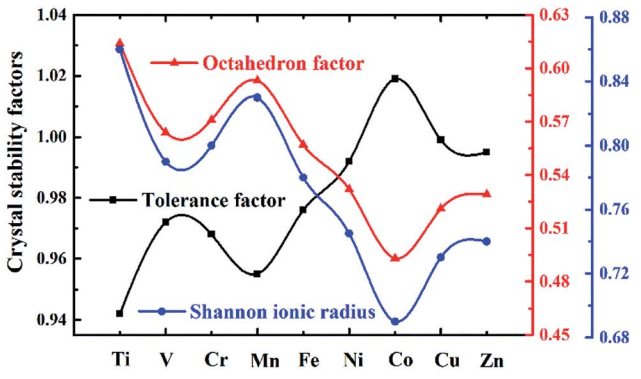

Fig. 2 Blue line with dots symbolizes Shannon ionic radius (Å) for 3d TM cations; black line with squares for tolerance factor and red line with triangles for octahedron factor are adopted for crystal stability evaluation.

Electronic structures

Firstly, band structure of 2 × 2 × 2 supercells of intrinsic cubic $KNbO_3$ (40 atoms) are calculated using the HSE06 functional to consider non-local effect typically important in metal oxides. The resultant direct band gap of 2.74 eV, Fig. 4a, which is slightly larger than the outcome from previous assessment (2.65 eV).[48] Partial densities of states show that O 2p states located at around −0.3 eV define the valence band maximum (VBM), and Nb 3d states at 2.4 eV determine the conduction band minimum (CBM),[55] while the states from K do not contribute to the bandgap value due to its being located at deep energy levels, as shown in Fig. 4b. For total DOS of $KNbO_3$, the spin-up states are compensated by spin-down states, leading to zero magnetism.

Fig. 5 illustrates three phases for the splitting of degenerate states of the octahedral centre atom under different conditions. Here the degenerate d^{10} shell configuration (phase I) is taken as an example to explain the following splitting process. Each orbital is occupied by two electrons with opposite spin orientation under the Hund rule and Pauli exclusion principle. Under the impact of crystal field theory, original fivefold degenerate states split into double degenerate states e_g (d_z^2 and

Table 1 Summary of band gap, transition path, gap character, application and magnetism after calculations, and conductivity characteristics (n- or p-type)

	Ti	V	Cr	Mn	Fe	Co	Ni	Cu	Zn
E_g (eV)	2.586	1.081	2.577	0.847	1.250	2.694	2.965	1.950	3.726
Transition path	G → G	R → G	M → G	R → G	R → G	M → G	M → G	R→G	G→G
Character	n	n	n	—	n	—	p	p	—
Application	TCO	PV	TCO	PV	PV	—	TCO	PV	—
Shell	$3d^24s^2$	$3d^34s^2$	$3d^54s^1$	$3d^54s^2$	$3d^64s^2$	$3d^74s^2$	$3d^84s^2$	$3d^{10}4s^1$	$3d^{10}4s^2$
Orbit		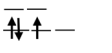	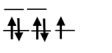						
μ_B (B. M.)	0.494	2.302	3.497	4.996	0.002	0.818	1.998	0.998	0

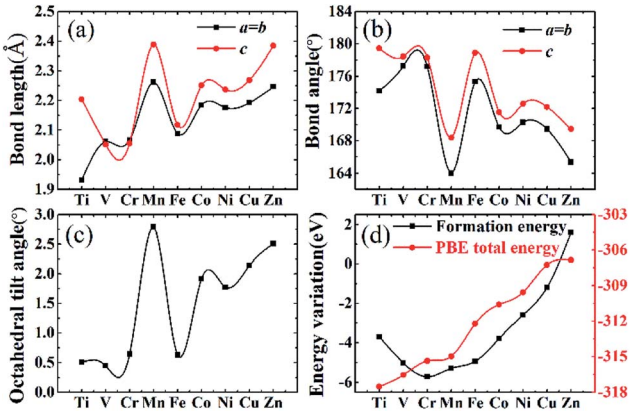

Fig. 3 (a) and (b) refer to bond length and bond angle from B′ dopant and the nearest oxygen, black line with blocks for *a* and *b* axes variation and red line with dots for *c* axis. (c) Maximum tilt angle of $B'O_6$ octahedron with respect to a neighbouring NbO_6 octahedron. (d) The energy variation including formation energy and total energy.

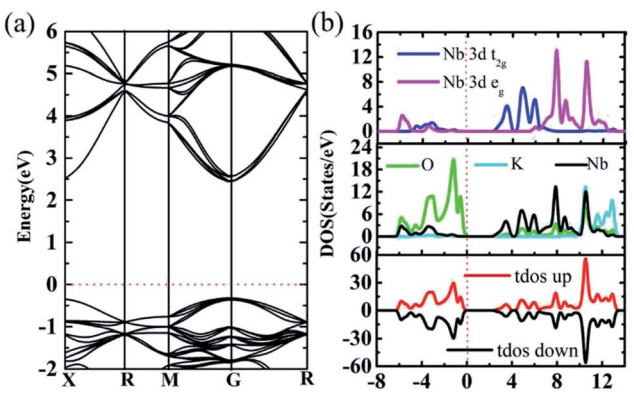

Fig. 4 (a) $KNbO_3$ band structure from HSE06 calculation with direct 2.74 eV band gap. (b) $KNbO_3$ total and partial DOS from HSE06 calculation. The high symmetry paths for cubic $KNbO_3$ are X (0.5, 0, 0), R (0.5, 0.5, 0.5), M (0.5, 0.5, 0), G (0, 0, 0) and R (0.5, 0.5, 0.5).

$d_{x^2-y^2}$) with higher energy level and threefold degenerate states t_{2g} (d_{xy}, d_{yz} and d_{xz}) with lower energy level. Normally the stretch direction of t_{2g} orbitals are along the diagonal directions between every two coordinate axes, resulted in t_{2g} orbitals

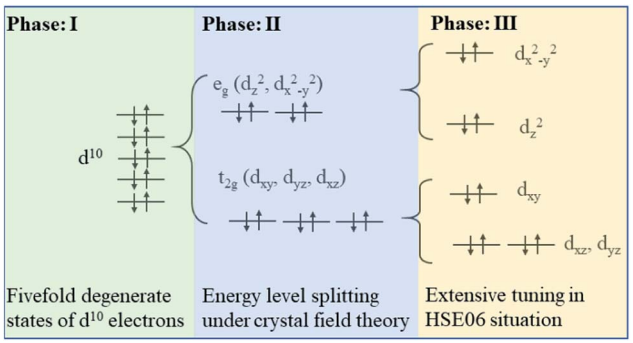

Fig. 5 The schematic diagram of TM $3d^{10}$ fivefold degenerate states splitting under crystal field and non-local effect in HSE06.

usually possessing lower energy with respect to these of e_g orbitals. Interestingly, degenerate e_g and t_{2g} states will be further split using a hybrid functional such as HSE06, thus resulting in more independent states contributing to electronic structures, where e_g states split into higher $d_{x^2-y^2}$ and lower d_z^2 states and t_{2g} states develop into higher d_{xy} and double degenerate d_{yz} and d_{xz} states along the *c* axis with lower energy. Such an effect is termed as extensive tuning from previous work on the non-degeneration states owing to anion substitution in the octahedron cage.[56]

The electronic polarization is considered in the calculation of electronic structures, with bands of different spin characters presented in red and black respectively in the band structures, Fig. 6. Spin-polarized band structures and associated total and partial density of states (Fig. 7) are combined to assess the effect of impurity states on the overall electronic structures:

Ti doping effect. The valence electrons of Ti occupy the 4s (2 electrons) and 3d shells (2 electrons), so that maximum valency of Ti is +4 such as in TiO_2. The nominal valency that substitutes the body centred Nb in one of the basic unit cells is 2.14, and that for the nearest neighbouring O is −1.21 from Bader charge analysis in Table S3.† This is understandable to consider that the bonding between O and metals are partially covalent. If one uses −2 nominal valency for O as reference for fully ionic compounds as a ruler for charge transfer, the effective valency for Ti cation in the supercell is +3.54, as compared to effective valency for other elements in the supercell, namely Ba (+2.56), K (+1.34), Nb (+4.26), and O (−2). This is suggestive that the

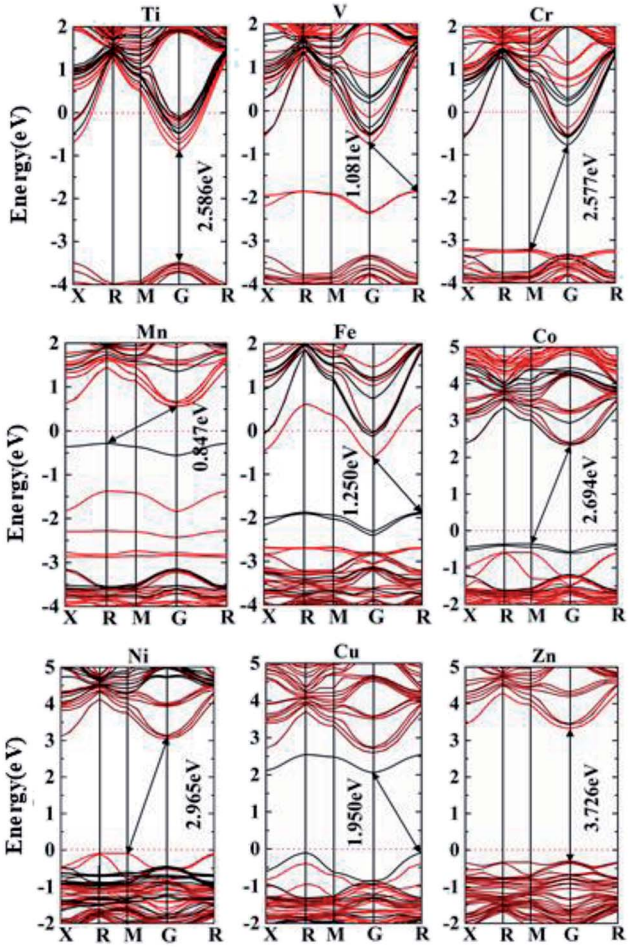

Fig. 6 Spin-polarized band structures from HSE06 calculation from Ti–Zn doped systems, red and black lines compose of spin-up bands and spin-down bands, respectively. The high symmetry paths for cubic $KNbO_3$ are X (0.5, 0, 0), R (0.5, 0.5, 0.5), M (0.5, 0.5, 0), G (0, 0, 0) and R (0.5, 0.5, 0.5).

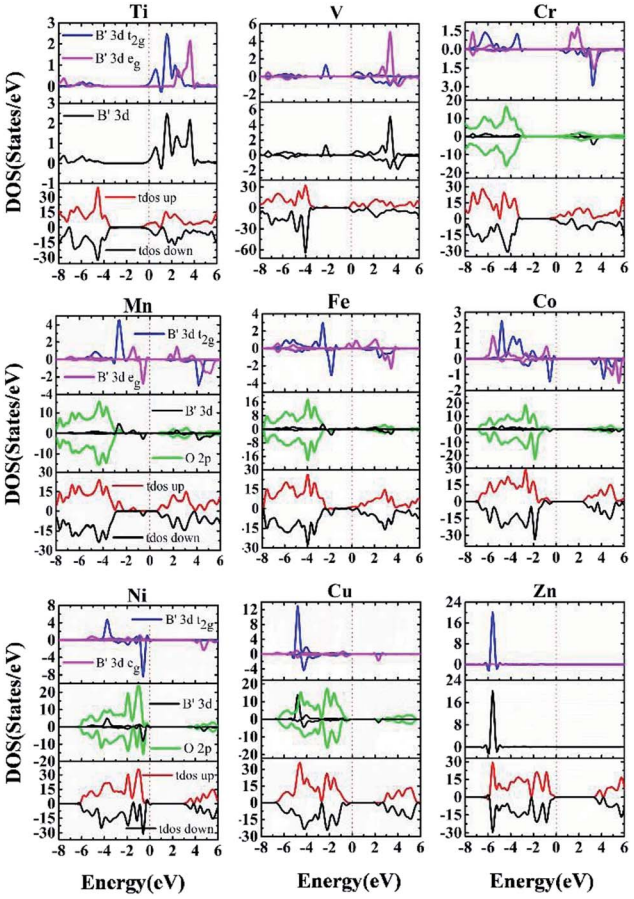

Fig. 7 Spin-polarized total and partial DOS from HSE06 calculation from Ti–Zn doped systems. The top chart plots their spin-up and spin-down partial DOS from B′ 3d e_g and t_{2g} states; the middle chart for B′ 3d and O 2p total DOS and the last chart for total DOS from the whole system.

valency electrons on more localized d-orbitals tend to be less prone to transferring charges to the neighbouring O anions. With only two 3d electrons, the 3d-shell of Ti is far from the stable and fully filled $3d^{10}$ state, and thus the e_g and t_{2g} states are split far apart in the conduction band, as shown in the partial density of states for Ti. The CBM is defined by the t_{2g} valence states of Ti, while the VBM is defined by O 2p states. The overall shapes in the conduction and valence bands are largely similar to that of the virgin host phase. The overall shift of CBM below the Fermi energy is indicative of n-type characteristics, and the clean gap from of mid-gap states helps for good transparency, especially when a much lower doping level is adopted. The highly pronounced curvature at the CBM suggests very good electron mobility. Slight redshift for optical absorption will be induced due to band gap narrowing for 0.154 eV.

V doping effect. The unpaired 3d electrons leads to spin polarization in V-doped material, which is reflected in spin polarization in both the t_{2g} and e_g, owing to degeneration of $3d_{xz}$ and $3d_{yz}$ states. Two nondegenerate t_{2g} bands are pushed downwards to −2.0 eV in the forbidden gap, with the rest of high energy states remaining in the conduction band, as noticeable in the PDOS of V in Fig. 7. The presence of impurity bands within the forbidden gap will promote optical absorption due to provision of a stepping stone for the relay of valence electrons into conduction band. The effective valency for V doped to the Nb position is only +3.14, which is smaller than that of doped Ti (+3.54). The overall forbidden gap is narrowed by 0.177 eV.

Cr doping effect. Impurity bands overlap with O 2p states at the VBM, with hybridization of Cr spin-up $3d_{xy}$ and O spin-up 2p states. Overall effect to band structure is similar to Ti, with the CBM being shifted below the Fermi energy, leading to n-type characteristics. The band gap of 2.577 eV is only 0.163 eV narrower than that of the host phase, making it a promising candidate for TCO application.

Mn doping effect. The material is intrinsic in nature with Fermi level being well within the forbidden gap. There are also additional bands attributed to double and threefold degenerate states of 3d states from doped Mn. The evident curvatures associated with such bands are helpful in making use of them as stepping stones to promote effective optical absorption, which is essential for photovoltaic or photocatalytic

applications. A major difference in the band structure of Mn-doped phase is that the Fermi energy is between the CBM and the upper impurity band, so that the material becomes an intrinsic semiconductor in nature. The effective band gap in this case corresponds to R–G excitation, which is only 0.847 eV and thus makes the material highly promising as an intrinsic optical absorber for n–i–p architecture of solar cells.

Fe doping effect. The lower bands owing to Fe 3d spin-down states of degenerate d_{xz} and d_{yz} is located at the G point, which is 0.262 eV above the M point of VBM from hybridized states from spin-up d_{xz} and d_{yz} and O 2p states. The CBM is below the Fermi level for n-type characteristics. The lower mid-gap band within the forbidden gap (associated to the host phase) with pronounced curvatures helps for effective relaying of valency electrons to the conduction band. The significant reduction of the overall forbidden gap for 0.519 eV and an effective upper gap of 1.25 eV is also highly helpful for its being utilized as an effective optical absorber.

Co doping effect. Starting from the Co $3d^7$ shell configuration, the t_{2g} orbitals are fully filled, and the e_g orbitals begin to be occupied by an unpaired electron, leading to spin polarization. There is significant difference in the band structure from these doped with earlier transition metals. From Ti to Cr, O 2p states tend to dictate the VBM with some hybridization with 3d states within the valence band. In the case of Co doping, Co–O interaction get weaker due to more than half of 3d-orbitals being filled, leading to remarkable contribution of 3d states to the VBM. Occupation of higher energy e_g orbitals helps push conduction bands upwards with respect to the Fermi energy. In this case, the position of the Fermi energy is above the VBM, recovering the intrinsic characteristics similar to the host phase of $KNbO_3$. The effect on the band gap value is rather trivial, due to the impurity band becoming the effective valence band over that of the host phase.

Ni doping effect. Impurity bands at VBM are composed of Ni d_z^2 band and O 2p bands, with the VBM uplifted close to the Fermi energy level to enable p-type characteristics. The forbidden gap of 2.965 eV is free of mid-gap states, with blue shift of 0.216 eV. This is fundamental for a potential p-type TCO, with both hole conductivity and optical transparency being enhanced.

Cu doping effect. Complete filling of the d-shell leads to its being further stabilized at lower energy levels (t_{2g}) within the valence band, so that the VBM is dictated again by the O 2p states. The CBM is characterized by split e_g states. The band structure is free of gap states, and the forbidden gap (1.95 eV) is narrowed for about one third, owing to the impurity band offering the effective CBM, making it a promising candidate for effective optical absorber for photovoltaic applications.

Zn doping effect. With both d- and s-shells completely filled, both the VBM and CBM are defined by the O 2p and Nb 3d states, respectively. The complete TM 3d shell is pushed to the bottom of the valence band, making them into pseudo-core states. With increased bond lengths in an enlarged lattice, there is a significant extension of the forbidden gap for 0.986 eV, leading to an overall gap of 3.726 eV. As the position of the VBM is −0.291 eV below the Fermi energy, the material is of intrinsic conduction characteristics like the host phase. The rather large G–G direct gap makes a potential candidate for ultraviolet optoelectronic devices such as UV detectors.

In summary, being rather different from doping binary oxides such as TiO_2,[37–41,57,58] the doping effect of 3d transition metals into perovskite oxides is rather complex, owing to the presence of non-transition metals in the A sites. The overall effects on conducting characteristics and potential applications are presented in Table 1, such that early transition metal doping from Ti to V leads to n-type characteristics. The existence of mid-gap bands such as V-, Mn- and Fe-doped materials are expected to permit multi-wavelength absorption, making them potential candidates for PV or photocatalytic applications. Ni and Cu doping leads to p-type characteristics, making them quite interesting for p-type TCO and optical absorber for solar cells, respectively. Zn and Co doped materials are free of gap states, with intrinsic nature for their VBM being evidently below the Fermi energy like the host phase.

Effective carrier mass and mobility

Carrier mass and associated mobility are important for semiconductors, especially for those suitable either for TCO or effective PV materials. Here we examine their transport properties using a simple approach based on the deformation potential theory,[59]

$$\mu = \frac{(8\pi)^{1/2}\hbar^4 e c_{ii}}{3(m^*)^{5/2}(k_B T)^{3/2} {E_1}^2} \quad (3)$$

where $\hbar$ is reduced Planck constant; e for electronic charge; $c_{ii} = V_0\left(\frac{\partial^2 E}{\partial V^2}\right)$ for the elastic constant, V_0 is the lattice volume; m^* for the carrier effective mass (inversely proportional to the band curvature at CBM or VBM for electrons and holes, respectively); k_B for the Boltzmann constant; T for temperature (300 K). $E_1 = \frac{\Delta E_{BM}}{\Delta V/V_0}$ for the deformation potential, the energy shifting of the band edge with respect to the volume variation (ΔV) along the original lattice (V_0).

We consider effective electron masses and mobilities for Ti and Cr doped systems for their donor characteristics (n-type), and effective masses of holes are evaluated for Ni and Cu doped systems with acceptor characteristics (p-type) in Table 2. The CBM for Ti or Cr doped materials are located at the G point, which shows remarkable curvature along the $(\bar{1}\bar{1}0)$ and (111) directions in the reciprocal space, Fig. 6. Radical shift of CBM down below the Fermi energy is induced owing to replace 1/8 of the Nb species in the 2 × 2 × 2 supercell (40 atoms), making the semiconductor into degenerated metallic phases. This provides a fundamental basis for a large scope of tuning of carrier concentration, by adjusting the percentage of substituted Nb in the material, *e.g.* from 1% up to 12.5% (1/8). The lower percentages of Nb substitution important to practical doping levels are too big for tractable investigation using hybrid functionals such as the HSE06, *e.g.* 3.7% Nb substitution already involves 27 unit-cells of perovskite (135 atoms). It

Table 2 Summary of effective masses and mobilities (10^4 cm^2 V^{-1} s^{-1}) for Ti, Cr, Ni and Cu doped systems, along with the corresponding orientation. The electron and hole mobilities for Si are 1500 and 450 cm^2 V^{-1} s^{-1}, respectively

	Ti (n)		Cr (n)		Ni (p)			Cu (p)		
	$(\bar{1}\bar{1}0)$	(111)	$(\bar{1}\bar{1}0)$	(111)	(011)	$(\bar{1}\bar{1}0)$	(111)	(011)	$(00\bar{1})$	(111)
m^*/m_0	0.02	0.03	0.02	0.03	0.24	0.03	0.17	0.11	0.05	0.03
μ	613.58	273.93	488.27	242.56	1.09	210.33	2.39	6.81	71.77	257.29

is worth mentioning that the overall doping effect at lower doing levels would be similar, except for lower density of states and narrower impurity bands. Such doping concentration effect was studiously demonstrated previously in Mn- or Zn-doped TiO_2.[38,40]

The effective electron masses are about the same in Cr or Ti doped materials, being 0.02 along the $(\bar{1}\bar{1}0)$ direction and 0.03 along (111), in the reciprocal space. This leads to very high electron mobility, such that for Ti doped perovskite, the mobility in the $(\bar{1}\bar{1}0)$ direction is over 4000 times of that in Si (1500 cm^2 V^{-1} s^{-1}). The direct band nature of the material provides great leverage for its use as a n-type semiconductor in diodes for various applications, when doping level is low. At heavier doping level, the material is to be highly attractive as a TCO based on sustainable materials resources, so that resource crisis due to the depletion of indium metal for ITO can be addressed with a promising alternative. For the Ni and Cu doped materials, one notes that evident lifting of the VBM with reference to the case of the host material, indicating tendency for p type characteristics. Ni doping leads to VBM to appear at the M point (0.5, 0.5, 0), with curvature towards the G point direction being much more pronounced than that towards the R point (0.5, 0.5, 0.5). The corresponding directions in the reciprocal space are (011), $(\bar{1}\bar{1}0)$ and (111), respectively. The maximum hole mobility in the $(\bar{1}\bar{1}0)$ direction is also over 4600 times of that in silicon. For Cu doped material, the VBM is at the R point (0.5, 0.5, 0.5). In this case, the curvatures towards both the X (0.5, 0, 0) and M (0.5, 0.5, 0) points are very high, corresponding to the directions of (011) and $(00\bar{1})$. Again, the maximum hole mobility along (111) is thousands of times bigger than that in silicon. Therefore, the Ni doped material would be expected to be a superb p-type TCO yet missing, and the Cu doped material with remarkably reduced band gap would be a potential candidate for effective photovoltaic applications.

Comparing to reported data, the carrier mobilities over $\sim 10^6$ cm^2 V^{-1} s^{-1} is in the same order of theoretically predicted data in superb two-dimensional materials.[60] They are significantly higher than reported experimental data in hybrid perovskites. For example, measured hole mobility in $CH_3NH_3PbI_3$ was 164 ± 25 cm^2 V^{-1} s^{-1} and the experimentally measured electron mobility in (Ba, La)SnO_3 (TCO) was 320 cm^2 V^{-1} s^{-1}.[61,62] The theoretically reported carrier mobilities for electrons and holes in $CH_3NH_3PbI_3$ are 7000–30 000 cm^2 V^{-1} s^{-1} and 1500–5500 cm^2 V^{-1} s^{-1} respectively.[63] It is generally observed that theoretically predicted carrier mobilities could be significantly bigger than experimentally reported values, due to existence of various structural defects in real materials.

Conclusion

First-principle modelling in the framework of the density functional theory has been carried out to study the effect of 3d transition metal (B′) doping to perovskite materials based on $KNbO_3$, *i.e.* $(KNbO_3)_{5/8}$-$(BaNb_{2/3}B'_{1/3}O_3)_{3/8}$.

Unlike in binary oxides such as TiO_2, the doping effect into perovskite is rather complex. In the simplest case such as doping with earlier transition metals Ti and Cr, the CBM is shifted effectively downwards with electron mobilities thousands of times higher than that in silicon. This makes them remarkable candidates for TCO alternatives using sustainable resources.

The middle transition metals such as Mn and Fe tend to bring about intermediate bands within the forbidden gap. Unpaired valence electrons with associated spin polarization promotes non-degenerated orbital occupation, which in turn helps formation of gap states, so that intermediate bands appear in V, Mn and Co doped materials. The presence of curvy intermediate bands within the forbidden gap would enhance optical absorption, as multi-wavelength absorption is enabled owing to optically relaying effect. This opens potential use of the materials for photovoltaic or photocatalytic applications.

Later transition metal Ni and the noble metal Cu bring about p-type characteristics together with very large hole mobility. Ni doping is of great potential as a p-type TCO yet missing in the semiconductor family, and Cu doped materials is considered to be a potential material for high performance solar cells.

Conflicts of interest

There are no conflicts to declare.

Acknowledgements

This work was funded in part by Zhengzhou Materials Genome Institute, the National Natural Science Foundation of China (No. 51001091, 111174256, 91233101, 51602094, and 11274100), and the Fundamental Research Program from the Ministry of Science and Technology of China (No. 2014CB931704). YL thanks Dr Zhuo Wang for technical training and helpful discussions.

Notes and references

1 W. Shockley and H. Queisser, *J. Appl. Phys.*, 1961, **32**, 510.
2 M. A. Green, *Prog. Photovolt: Res. Appl.*, 2009, **17**, 183–189.
3 A. Kojima, K. Teshima, Y. Shirai and T. Miyasaka, *J. Am. Chem. Soc.*, 2009, **131**, 6050–6051.
4 A. B. Yusoff, P. Gao and M. K. Nazeeruddin, *Coord. Chem. Rev.*, 2018, **373**, 258–294.
5 A. Abate, *Joule*, 2017, **1**, 659–664.
6 M. R. Filip, S. Hillman, A. A. Haghighirad, H. J. Snaith and F. Giustino, *J. Phys. Chem. Lett.*, 2016, **7**, 1254–1259.
7 X. G. Zhao, D. W. Yang, J. C. Ren, Y. H. Sun, Z. W. Xiao and L. J. Zhang, *Joule*, 2018, **2**, 1–12.
8 H. J. Zhang, G. Chen, X. D. He and J. Xu, *J. Alloys Compd.*, 2012, **516**, 91–95.
9 H. J. Zhang, G. Chen, Y. X. Li and Y. J. Teng, *Int. J. Hydrogen Energy*, 2010, **35**, 2713–2716.
10 R. B. Comes, P. V. Sushko, S. M. Heald, R. J. Colby, M. E. Bowden and S. A. Chambers, *Chem. Mater.*, 2014, **26**, 7073–7082.
11 T. Onishi, *Top. Catal.*, 2010, **53**, 566–570.
12 F. Yang, L. Yang, C. Z. Ai, P. C. Xie, S. W. Lin, C. Z. Wang and X. H. Lu, *Nanomaterials*, 2018, **8**, 455.
13 Z. Teng, J. J. Jiang, G. Y. Chen, C. L. Ma and F. W. Zhang, *AIP Adv.*, 2018, **8**, 095216.
14 I. Masuda, K. I. Kakimoto and H. Ohsato, *J. Electroceram.*, 2004, **13**, 555–559.
15 J. A. Astudillo, S. A. Dionizio, J. L. Izquierdo, O. Moŕan, J. Heiras and G. Bolãnos, *AIP Adv.*, 2018, **8**, 055817.
16 W. Cai, C. L. Fu, R. L. Gao, W. H. Jiang, X. L. Deng and G. Chen, *J. Alloys Compd.*, 2014, **617**, 240–246.
17 T. Choi, S. Lee, Y. J. Choi, V. Kiryukhin and S. W. Cheong, *Science*, 2009, **324**, 63.
18 M. L. Cohen, *Science*, 1993, **261**, 307–308.
19 I. Grinberg, D. V. West, M. Torres, G. Y. Gou, D. M. Stein, L. Y. Wu, G. N. Chen, E. M. Gallo, A. R. Akbashev and P. K. Davies, *Nature*, 2013, **503**, 509–512.
20 W. L. Zhou, H. M. Deng, P. X. Yang and J. H. Chu, *Appl. Phys. Lett.*, 2014, **105**, 111904.
21 W. L. Zhou, H. M. Deng, L. Yu, P. X. Yang and J. H. Chu, *J. Phys. D: Appl. Phys.*, 2015, **48**, 455308.
22 W. L. Zhou, H. M. Deng, L. Yu, P. X. Yang and J. H. Chu, *Mater. Lett.*, 2017, **202**, 39–43.
23 L. M. Yu, J. H. Jia, G. W. Yi, Y. Shan and M. M. Han, *Mater. Lett.*, 2016, **184**, 166–168.
24 S. F. Si, H. M. Deng, W. L. Zhou, T. T. Wang, P. X. Yang and J. H. Chu, *Ceram. Int.*, 2018, **44**, 14638–14644.
25 Q. F. Zhang, F. Xu, M. J. Xu, L. Li, Y. M. Lu, M. K. Li, P. Li, M. Li, G. Chang and Y. B. He, *Mater. Res. Bull.*, 2017, **95**, 56–60.
26 R. P. Tiwari, J. Shah, R. K. Kotnala and B. Birajdar, *J. Alloys Compd.*, 2018, **753**, 642–645.
27 B. Q. Song, X. J. Wang, C. Xin, L. L. Zhang, B. Song, Y. Zhang, Y. Wang, J. Wang, Z. G. Liu, Y. Sui and J. K. Tang, *J. Alloys Compd.*, 2017, **703**, 67–72.
28 F. G. Wang, I. Grinberg and A. M. Rappe, *Phys. Rev. B: Condens. Matter Mater. Phys.*, 2014, **89**, 235105.
29 C. Lohaus, C. Steinert, G. Deyu, J. Brötz, W. Jaegermann and A. Klein, *Appl. Phys. Lett.*, 2018, **112**, 152105.
30 I. Hamberg and C. G. Granqvist, *J. Appl. Phys.*, 1986, **60**, R123–R160.
31 G. G. Untila, T. N. Kost and A. B. Chebotareva, *Sol. Energy*, 2018, **159**, 173–185.
32 S. Y. Liu, S. Liu, Y. Y. Zhou, Y. J. Piao, G. J. Li and Q. Wang, *Appl. Phys. Lett.*, 2018, **113**, 032102.
33 L. Lu, M. L. Guo, S. Thornley, X. Han, J. H. Hu, M. J. Thwaites and G. S. Shao, *Sol. Energy Mater. Sol. Cells*, 2016, **149**, 310–319.
34 B. H. Wang, W. Zhang, K. B. Yang, T. Liao, F. Z. Li, Y. Y. Cui, Y. F. Gao and B. Liu, *Ceram. Int.*, 2018, **44**, 16051–16057.
35 M. A. Riza, M. A. Ibrahim, U. C. Ahamefula, M. A. Mat Teridi, N. A. Ludin, S. Sepeai and K. Sopian, *Sol. Energy*, 2016, **137**, 371–378.
36 G. Kresse and J. Furthmller, *Comput. Mater. Sci.*, 1996, **6**, 15–50.
37 G. Shao, *J. Phys. Chem. C*, 2009, **113**, 6800–6808.
38 G. Shao, *J. Phys. Chem. C*, 2008, **112**, 18677.
39 X. P. Han, K. Song, L. Liu, Q. Deng, X. Xia and G. Shao, *J. Mater. Chem. C*, 2013, **1**, 3736.
40 X. P. Han and G. Shao, *Phys. Chem. Chem. Phys.*, 2013, **15**, 9581.
41 X. P. Han and G. Shao, *J. Mater. Chem. C*, 2011, **115**, 8274.
42 P. E. Blochl, *Phys. Rev. B: Condens. Matter Mater. Phys.*, 1994, **50**, 953–979.
43 J. P. Perdew, K. Burke and M. Ernzerhof, *Phys. Rev. Lett.*, 1996, **77**, 3865–3868.
44 J. Heyd, G. E. Scuseria and M. Ernzerhof, *J. Chem. Phys.*, 2003, **118**, 8207–8215.
45 J. Heyd, G. E. Scuseria and M. Ernzerhof, *J. Chem. Phys.*, 2006, **124**, 219906.
46 J. Paier, M. Marsman, K. Hummer, G. Kresse, I. C. Gerber and J. G. Angyan, *J. Chem. Phys.*, 2006, **124**, 154709.
47 M. Marsman, J. Paier, A. Stroppa and G. Kresse, *J. Phys.: Condens. Matter*, 2008, **20**, 064201.
48 F. Wang and A. M. Rappe, *Phys. Rev. B: Condens. Matter Mater. Phys.*, 2015, **91**, 165124.
49 C. L. Diao and H. W. Zheng, *J. Mater. Sci.: Mater. Electron.*, 2015, **26**, 3108–3111.
50 G. Kresse, M. Marsman, and J. Furthmuller, *VASP the GUIDE*, 2009, pp. 61–135.
51 Z. Li, M. J. Yang, J. S. Park, S. H. Wei, J. J. Berry and K. Zhu, *Chem. Mater.*, 2016, **28**, 284–292.
52 Z. W. Xiao and Y. F. Yan, *Adv. Energy Mater.*, 2017, **7**, 1701136.
53 R. Q. Wu, *J. Appl. Phys.*, 2002, **91**, 7358.
54 W. Y. Yu, Z. L. Zhu, C. Y. Niu, C. Li, J. H. Cho and Y. Jia, *Nanoscale Res. Lett.*, 2016, **11**, 77.
55 T. Neumann, G. Borstel, C. Scharfschwerdt and M. Neumann, *Phys. Rev. B: Condens. Matter Mater. Phys.*, 1992, **46**, 10623–10628.

56 H. Kageyama, K. Hayashi, K. Maeda, J. P. Attfield, Z. Hiroi, J. M. Rondinelli and K. R. Poeppelmeier, *Nat. Commun.*, 2018, **9**, 772.
57 K. N. Song, X. P. Han and G. Shao, *J. Alloys Compd.*, 2013, **551**, 118–124.
58 Q. R. Deng, X. P. Han, Y. Gao and G. Shao, *J. Appl. Phys.*, 2012, **112**, 013523.
59 J. Bardeen and W. Shockley, *Phys. Rev.*, 1950, **80**, 72–80.
60 E. H. Hwang and S. D. Sarma, *Phys. Rev. B: Condens. Matter Mater. Phys.*, 2007, **11**, 77.
61 Q. F. Dong, Y. J. Fang, Y. C. Shao, P. Mulligan, J. Qiu, L. Cao and J. S. Huang, *Science*, 2015, **347**, 967–970.
62 H. J. Kim, U. Kim, T. H. Kim, J. Kim, H. M. Kim, B. G. Jeon, W. J. Lee, H. S. Mun, K. T. Hong and J. Yu, *Phys. Rev. B: Condens. Matter Mater. Phys.*, 2012, **86**, 16.
63 Y. W. Wang, Y. B. Zhang, P. H. Zhang and W. Q. Zhang, *Phys. Chem. Chem. Phys.*, 2015, **17**, 11516–11520.